CCFE-PR(16)49

Zhaoyuan Leong, Jan S. Wróbel, Sergei L. Dudarev, Russell Goodall, Iain Todd,
and Duc Nguyen-Manh

The Effect of Electronic Structure on the Phases Present in High Entropy Alloys

The Effect of Electronic Structure on the Phases Present in High Entropy Alloys

Zhaoyuan Leong[1], Jan S. Wróbel[2,3], Sergei L. Dudarev[2], Russell Goodall[1], Iain Todd[1], Duc Nguyen-Manh[2]

[1]Department of Materials Science & Engineering, University of Sheffield, Sheffield, U.K.
[2]CCFE, Culham Science Centre for Fusion Energy, Culham, Abingdon, OX14 3DB, Oxfordshire, U.K.
[3]Faculty of Materials Science and Engineering, Warsaw University of Technology, ul. Wołoska 141, 02-507 Warszawa, Poland.

The Effect of Electronic Structure on the Phases Present in High Entropy Alloys

Zhaoyuan Leong[1*], Jan S. Wróbel[2,3], Sergei L. Dudarev[2], Russell Goodall[1], Iain Todd[1], Duc Nguyen-Manh[2**]

[1]Department of Materials Science & Engineering, University of Sheffield, Sheffield, U.K.
[2]CCFE, Culham Science Centre for Fusion Energy, Culham, Abingdon, OX14 3DB, Oxfordshire, U.K.
[3]Faculty of Materials Science and Engineering, Warsaw University of Technology, ul. Wołoska 141, 02-507 Warszawa, Poland.

Corresponding authors:
*zhaoyuan@sheffield.ac.uk; **duc.nguyen@ukaea.uk

Abstract

Multicomponent systems with predominantly simple phases are an area of current focus in alloy development. Termed High Entropy Alloys (HEAs), different empirical rules have been introduced to understand phase formation in these systems, and determine what the dominant phases may be. However, experimental investigation has revealed that in many cases their structure is not a single simple phase, and may not be fully stable. It is therefore surprising that there is a degree of success in models largely based on fundamental thermodynamic and atomic parameters. To understand this, a combined modelling and experimental approach is proposed by generalising a Rigid Band model for magnetic systems and taking electronic structure effects into account in prediction of the phase most likely to be found in multicomponent alloys. Good agreement is found when the predictions are confronted with data from experiments, including a new magnetic HEA system (CoFeNiV). This also includes predicting the structural transition with varying levels of constituent elements, as a function of the valence electron concentration, *n,* obtained from the integrated spin-polarised density of states. This method is suitable as a new predictive technique to identify compositions for further screening, in particular for magnetic HEAs.

Introduction

In the continuing search for new alloys, a recent trend has been to move away from systems dominated by a single element with minor additions towards alloys consisting of multiple elements in similar quantities. These alloys were expected to show multiple complex phases, and hence be of limited use, but experimental evidence has shown that some such alloys, called High Entropy Alloys (HEAs)[1–4], frequently form simple phases. They were first observed in the five-component equiatomic alloy CoCrFeNiMn (here denoted CCFN-$Mn_{1.0}$, as the base composition CoCrFeNi occurs widely in these alloys)[1] forming a face-centred cubic (FCC) phase. Further experiments suggested that such phases resisted ordering[2] , which was attributed to stabilisation by chemical and magnetic contributions to the entropy resulting from the multiple components[5,6] (although this is disputed as the sole, or even primary, cause[7]). Investigation of the properties of such alloys highlighted a number of attractive features (such as high strength combined with ductility) which makes the design of alloys using the effect, whatever the cause, desirable[4].

Most of the experimental studies of these alloys make use of processing methods, such as arc melting, likely to give non-equilibrium conditions for phase formation. More recent studies of some alloys have found that many are not simply single phase, or stable against transformation. For example, it has been found that on heat treatment, additional complex phases form in CCFN-$Mn_{1.0}$[8], and that other alloys, (including several CCFN-A type alloys and the 4-component alloy CCFN itself) are not homogenous on the atomic scale and perfect solid solutions are not obtained[9,10].

Nevertheless, many attempts have been made to discriminate between compositions for which simple phases apparently occur and those where they do not. Empirical rules have met with some success, including utilising the Hume-Rothery rules[11] to relate the Valence Electron Concentration (VEC) to the phase formed[12], and the Miedema model to investigate solid-solution stability[13]. Using a

Principal Component Analysis (PCA) method, Dominguez *et al.*[14] analysed the contributions of five thermodynamic and electronic variables (enthalpy of mixing, entropy of mixing, atomic size mismatch, electronegativity difference, and VEC) and found that different simple structures and intermetallic compounds are reasonably well differentiated by the values of VEC and the Enthalpy of Mixing of the alloy; other factors identified in previous work[12,14,15]such as the electronegativity difference, atomic size difference, and the configurational entropy of solid solutions were found to have a lesser influence on phase stability.

Although this framework offers differentiation between the simple phases FCC and BCC, the occurrence of simple and complex phases is not discriminated, and the accuracy of these empirical rules appears to be strongly dependent on the amount of alloying additions[12], limiting the extent to which alloy compositions can be designed. The solution may be to consider the electronic structure, the effects of which are not fully captured by the empirical approaches. To access such information, the Density Functional Theory (DFT) formalism[16] can be used, such as in investigating enthalpies[17] and entropies[18] of formation for HEAs within spin-polarised electronic structure calculations. One simplification of the DFT approach is the Rigid Band Approximation (RBA), originally proposed for non-magnetic metallic alloys, which assumes that the energy difference between two phases is given entirely by the difference in band-structure energy[19–22]. This allows the study of the structural energy difference, and hence prediction of the most stable phase, in a computationally less intense manner than full DFT calculations. It has been successfully implemented for different alloy systems[19–22], though not previously for HEAs. The RBA models are simple enough to readily interpret the available experimental data yet powerful enough to correctly predict the new stable phase in a multicomponent system.

In order to better understand, and improve on, the phase discrimination found in 2-dimensional plots of the empirical models[14], we experimentally investigate the transition from simple to complex phases of a number of 5-component HEA alloys based on the equiatomic CoCrFeNi (CCFN) composition through X-Ray Diffraction (XRD) characterisation. The compositions are compared to predictions from the RBA approach, in particular of the transition between phases that occurs with changing stoichiometry. We generalise the original RBA approach[19-20] to include the effects of magnetism using the Stoner model[23–27], as this affects the change in energy between two phases (particularly since the constituent metals Co, Cr, Fe, and Ni already exhibit magnetic behaviour; other CoCrFeNi-type alloys have also been reported for their magnetic properties[18,28–30]). It is found that the VEC parameter is able to serve as a good predictor of simple-complex transitions when the s, p, and d valence electrons are accounted for. Therefore the RBA model can be used as a simple but relatively accurate method based on electronic structure calculations for phase stability prediction in HEAs as will be demonstrated within this paper, in particular in the understanding and design of alloys in the new CoFeNiV system.

Results

Experimental Identification of Phases Adopted by CoCrFeNi-type Compositions

20 HEA compositions based on $CoCrFeNiA_X$, where A = Pd, Al, V, and Ti (henceforth denoted as CCFN-Pd_x, CCFN-Al_x, CCFN-V_x, and CCFN-Ti_x) with nominal compositions given in Table 1, were made. The amount of each addition was selected to explore the transition between simple (FCC and BCC) and complex (B2, Sigma and C14) phases. We have extended the analysis of CCFN-A_x compositions beyond those previously reported to identify the accuracy of the RBA-predicted phase stability in terms of the relative behaviour of the electronic densities of states.

Table 1. High Entropy Alloy compositions with their respective nominal compositions, indexed phases and lattice constants, and VEC values.

*These new stoichiometric compositions have been selected to extend the literature data on the CCFN-A (A = Pd, V, Al, and Ti) compositional families selected for this work

Composition	Nominal Composition	Indexed Phase	Lattice Parameter (Å) +/- 0.01 Å	VEC	Reference
CCFN	CoCrFeNi	FCC	a = 3.56	8.25	[9,12,30]
CCFN-$Pd_{0.5}$	$(CoCrFeNi)_{0.89}Pd_{0.11}$	FCC	a = 3.62	8.44	[30]
CCFN-$Pd_{1.0}$	$(CoCrFeNi)_{0.80}Pd_{0.20}$	FCC	a = 3.66	8.60	[30]
CCFN-$Pd_{1.5}$	$(CoCrFeNi)_{0.73}Pd_{0.27}$	FCC	a = 3.71	8.73	This Work*
CCFN-$Al_{0.5}$	$(CoCrFeNi)_{0.89}Al_{0.11}$	FCC	a = 3.60	7.67	[31,32]
		BCC	a = 2.87		
CCFN-$Al_{1.0}$	$(CoCrFeNi)_{0.80}Al_{0.20}$	BCC	a = 2.88	7.20	[31,32]
CCFN-$Al_{1.5}$	$(CoCrFeNi)_{0.73}Al_{0.27}$	BCC	a = 2.88	6.81	[31,32]
		B2	a = 2.82		
CCFN-$Al_{3.0}$	$(CoCrFeNi)_{0.57}Al_{0.43}$	B2	a = 2.89	6.00	This Work*
CCFN-$V_{0.3}$	$(CoCrFeNi)_{0.93}Al_{0.07}$	FCC	a = 3.58	8.02	This Work*
CCFN-$V_{0.7}$	$(CoCrFeNi)_{0.85}V_{0.15}$	FCC	a = 3.59	7.77	This Work*
		Sigma	a = 8.78 c = 4.60		
CCFN-$V_{1.0}$	$(CoCrFeNi)_{0.80}V_{0.20}$	FCC	a = 3.61	7.60	[33]
		Sigma	a = 8.79 c = 4.58		
CCFN-$V_{2.0}$	$(CoCrFeNi)_{0.67}V_{0.33}$	Sigma	a = 8.87 c = 4.59	7.17	This Work*
CoFN-$V_{1.0}$	$(CoFeNi)_{0.75}V_{0.25}$	FCC	a = 3.59	8.00	This Work*
CoFN-$V_{1.5}$	$(CoFeNi)_{0.67}V_{0.33}$	FCC	a = 3.61	7.67	This Work*
CoFN-$V_{2.0}$	$(CoFeNi)_{0.60}V_{0.40}$	Sigma	a = 9.04 c = 4.68	7.40	This Work*
CCFN-$Ti_{0.4}$	$(CoCrFeNi)_{0.91}Ti_{0.09}$	FCC	a = 3.59	7.86	This Work*
CCFN-$Ti_{0.6}$	$(CoCrFeNi)_{0.87}Ti_{0.13}$	FCC	a = 3.61	7.70	This Work*
CCFN-$Ti_{1.0}$	$(CoCrFeNi)_{0.80}Tl_{0.20}$	C14	a = 4.79 c = 7.76	7.40	[34]
		FCC	a = 3.64		
CCFN-$Ti_{1.5}$	$(CoCrFeNi)_{0.73}Tl_{0.27}$	C14	a = 4.77 c = 7.74	7.09	This Work*
CCFN-$Ti_{2.0}$	$(CoCrFeNi)_{0.67}Ti_{0.33}$	C14	a = 4.81 c = 7.82	6.83	This Work*
		BCC	a = 2.98		

Further compositions from the novel CoFeNiV$_x$ system (henceforth denoted CoFN-V$_x$) were also prepared in order to validate the use of the RBA model for unknown compositions against experimental data. The compositional variations are tabulated in Table 1.

To analyse the phases adopted by these compositions, XRD characterisation experiments were performed. The XRD patterns show that, within detection limits, the FCC phase is present for compositions CCFN-Pd$_{0.5}$, CCFN-Pd$_{1.0}$, and CCFN-Pd$_{1.5}$. For the CCFN-Al$_x$ family the FCC phase is maintained for CCFN-Al$_{0.5}$ with some small amounts of BCC/B2 formation. The BCC phase is fully adopted at the CCFN-Al$_{1.0}$ composition, with the BCC/B2 phases at CCFN-Al$_{3.0}$. Similarly, the CCFN-V$_x$ family shows FCC alone at the smaller V additions of CCFN-V$_{0.5}$ and CCFN-V$_{0.8}$ with some secondary phase formation for larger V additions. A mixed FCC-Sigma phase is observed for CCFN-V$_{1.0}$ and the composition fully adopts the Sigma phase by CCFN-V$_{2.0}$. The phase formation and Rietveld refined lattice parameters are summarised in Table 1; where increasing amounts of Pd, Al, and V are added to CCFN there is an associated increase in the lattice parameter.

Phase discrimination in a 2-dimensional plot of the enthalpy of mixing against VEC was first presented by Dominguez *et al.*[14], where a single BCC phase was identified for 3 < VEC < 6, a single FCC phase for 8 < VEC < 11, and complex phases at intermediate values (for 6 < VEC < 8). The empirical VEC for an alloy may be obtained from the weighted average of the electrons accommodated in the s, p, d orbitals of the alloy's constituent elements[12]. Our experimental results show that the compositions of complex phases (*c.f.* Table 1) indeed possess values in the intermediate range of 6 < VEC < 7.8. However, when considering the phase stability of complex structures in specific compositions, the cubic B2 presence in CCFN-Al$_x$ compositions determined experimentally is observed fully only from VEC ≤ 6.81; the tetragonal Sigma phase presence in the CCFN-V$_x$ compositions at VEC ≤ 7.77; and the hexagonal C14 phase presence in CCFN-Ti$_x$ compositions at VEC ≤ 7.4.

These observations highlight the behaviours that result from the dependence of electronic structure for the different complex phases on elemental alloy additions. The RBA method employed in this study allows investigation of the relative structural stability of CCFN (CCFN-A$_x$) as a function of the exact valence electron concentration, *n,* which is, in turn, obtained from the integration of the density of electronic states (*cf.* equation (2) below).

RBA Phase Stability as a Function of the Valence Electron Concentration

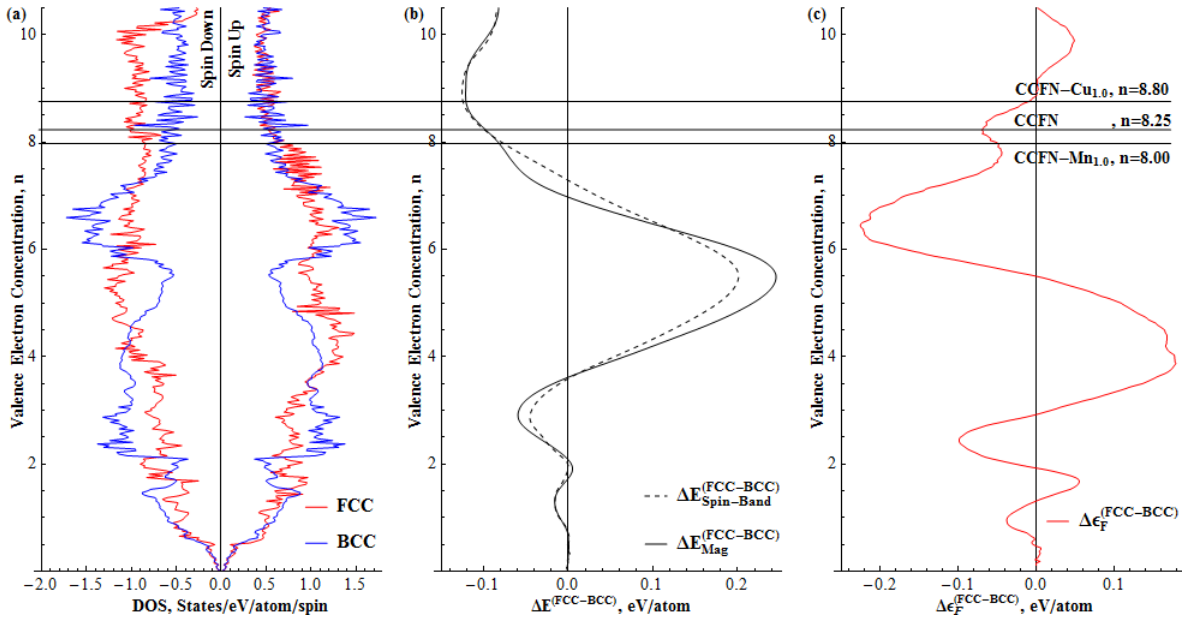

Figure 1. (a) Spin-polarised density of states of FCC and BCC 32-atom Special Quasi-Random Structure (SQS) CCFN and; **(b)** Spin-polarised band energy difference between FCC and BCC CCFN (i) Without double-counting Stoner corrections, (ii) With Stoner Correction and; **(c)** The Fermi energy difference between the FCC and BCC structure (*c.f.* equation (4)).

Within DFT, the total energy difference between two structures for a particular alloy (1 and 2) at a fixed volume can be decomposed into two contributions[19,35,36]**:**

$$\Delta E^{(1-2)} = \Delta E_B^{(1-2)} + \Delta E_{e-e}^{(1-2)} \quad (1)$$

where the first contribution represents the change in band energy between the two structures, and the second contribution arises from the structural energy difference in electrostatic and electron-electron interactions. By using the RBA/frozen potential approach[35,36], the energy difference between two non-magnetic phases can be simply evaluated by comparing the band-structure energy difference computed using the same frozen potential for the two structures at a fixed volume. This approximation is valid to the first order, not only for an elemental metal, but also for metallic alloys where the second contribution is considered to be small[19–22]. In order to analyse the phase stability over a wide range of concentrations the energy difference can be presented as a function of *n*, which can in turn be determined from the integration of the total electronic density of states (DOS) per atom up to the Fermi energy.

For magnetic alloys, such as CCFN-based HEAs investigated in this work, applying the Stoner model to the RBA allows the band energy difference to be decomposed to contributions from the spin-polarised band energy and the double-counting contributions arising from magnetic interactions[23,24,26,27]. In this case, the value of valence electron concentration, *n,* can be obtained from the integration of the spin-polarised total DOS per atom as

$$n = \int_{-\infty}^{\varepsilon_F} D^{\uparrow}(\varepsilon) d\varepsilon + \int_{-\infty}^{\varepsilon_F} D^{\downarrow}(\varepsilon) d\varepsilon = n_{\uparrow} + n_{\downarrow} \quad (2)$$

where $D^{\uparrow}(\varepsilon)$ and $D^{\downarrow}(\varepsilon)$ are the spin-polarised total DOS per atom for electrons with spin-up and spin-down, respectively, and ε_F is the Fermi energy.

Exact application of the Stoner model requires knowledge of magnetic moments of all atoms in the system but it can be simplified through using an effective Stoner parameter, I_{eff}. This is defined as the exchange splitting of the on-site energies of electrons with spin-up and spin-down due to average atomic magnetic moment, m_{av}, which can be obtained from the non-magnetic total DOS and the value of the average atomic magnetic moment of the entire simulation cell. The energy difference between any two magnetic structures can be thus written as:

$$\Delta E_{Mag}^{(1-2)} \approx \Delta E_{Spin-Band}^{(1-2)} + \frac{1}{4}\left[I_{eff}^{(1)} m_{av}^{2\,(1)} - I_{eff}^{(2)} m_{av}^{2\,(2)}\right] \quad (3)$$

where the first term is related to the spin-polarised band energy difference obtained from the total DOS per atom and per electron spin and the second term is the double-counting contribution coming from magnetic interactions. As shown in Table I in the Supplementary information, the energy differences calculated with a knowledge of magnetic moments of all atoms in the system and those obtained using average magnetic moments and effective Stoner parameters are in quantitative agreement and are in line with the results obtained using the LMTO code[37]. Thus, for the RBA analysis of stability of other CCFN-based alloys the simplified method based on the effective Stoner parameter will be applied. The derivation of the RBA for magnetic systems using the Stoner model can be found in the supplementary information [see equations (I-V)]. Fig. 1 (a) shows the spin-polarised DOS of disordered simple FCC and BCC phases calculated utilising a Special Quasi-

random Structure (SQS)[38,39]generated $Co_8Cr_8Fe_8Ni_8$ structure, representing the CCFN composition, which is used for the RBA analysis. Fig. 1 (b) shows the resulting FCC-BCC band energy difference of CCFN alloys calculated with and without Stoner corrections as a function of *n*.

From Fig. 1 (b) it is observed that the FCC phase for the CCFN composition is stabilised in the region of $n > 6.97$ according to the RBA prediction from equation (3). The FCC stable zone reported by Dominguez *et al.'s* PCA analysis was $8 < VEC < 11$[14]**;** this difference is expected as we have not considered the stability of complex phases in the CCFN composition. The compositions CCFN-Mn and CCFN-Cu (with $n = 8$ and $n = 8.8$ respectively) lie within the FCC-stable region; this RBA prediction is in agreement with experimental determination of their structures[1]. According to Fig. 1(b), the simple BCC phase would be stabilised within $3.75 < n < 6.97$. Extension of our RBA analysis to the experimental observation for BCC HEAs containing 4d and 5d BCC transition metals (TMs) previously reported such as WNbMoTa[40,41]with VEC = 5.5, and TiVMnNb[14] with VEC = 5.25 agrees with the RBA model as both fall within the BCC-stable region.

Below we apply the RBA model for studying the structural-stability competition between simple phases (FCC and BCC) and different complex phases within four CCFN-A_x alloys (A=Pd, Al, V and Ti).

I – CCFN-Pd

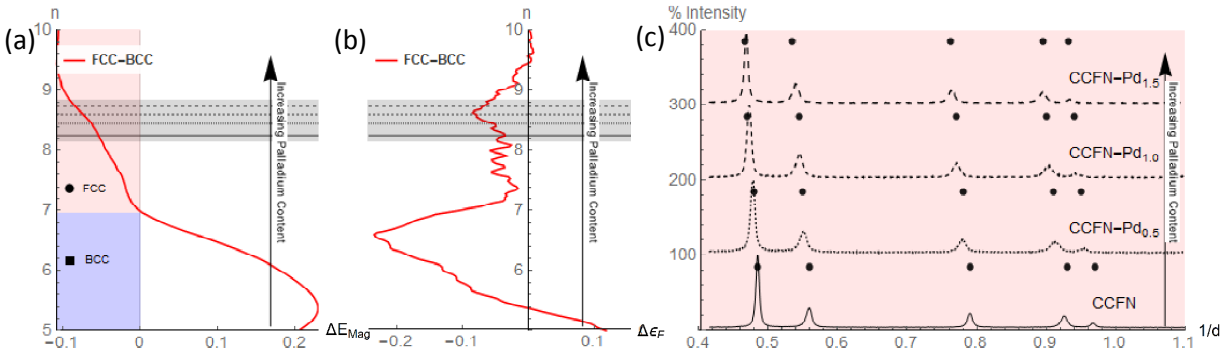

II – CCFN-Al

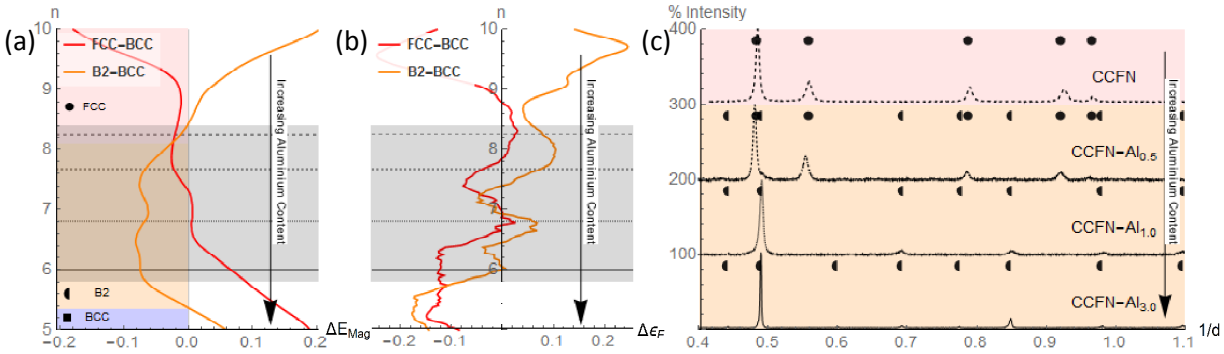

III – CCFN-V

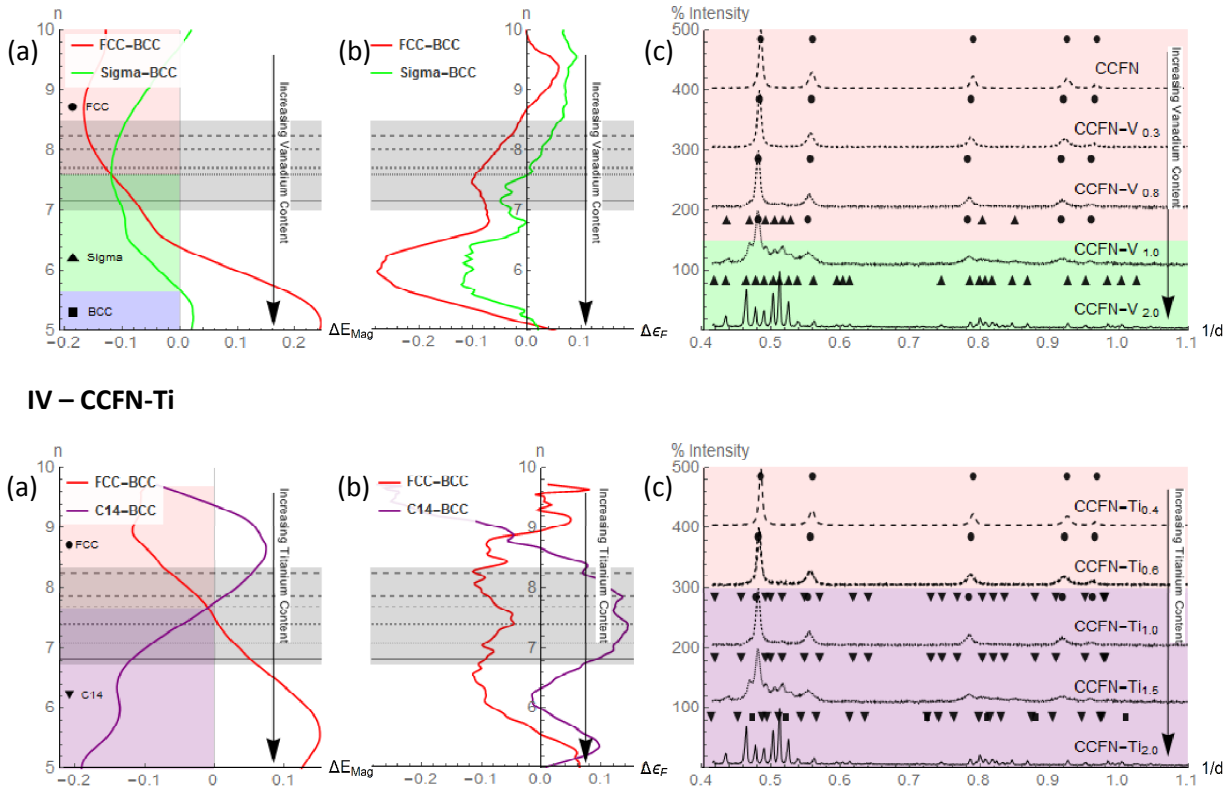

Figure 2. Predictions and experimental results for several alloy systems, I – CCFN-Pd, II – CCFN-Al, III –CCFN-V, and IV – CCFN-Ti, showing for each, the change in phase stability with increasing 5th element content through (a) VEC, *n*, against the band energy difference, (b) The Fermi Energy difference as defined in equation (4) below, and (c) Its associated XRD Patterns.

Fig. 2(I-IV) shows the results of theoretical and experimental investigation of phase stability of several 5-component CCFN-based alloy systems. In each case the fifth element was chosen to represent a different type of alloying element. In the CCFN-Pd alloys shown in Fig. 2I, palladium is a 4d-transition metal element located on a different row of the periodic table to the other four elements (Cr, Co, Fe and Ni; 3d transition metals). Accordingly, the results from the RBA model comparing the energy difference between FCC and BCC structures in CCFN-Pd alloys, shown in Fig. 2I, are slightly different to those for CCFN alloys displayed in Fig. 1. The RBA results for energy differences between the simple phases (FCC and BCC) and B2 phase in CCFN-Al alloys (where Al is a sp-metal from outside the transition metal series) are shown in Fig 2II. Finally, for CCFN-V and CCFN-Ti alloys, where both V and Ti are in the same 3d transition metal series, there is competition between simple and complex phases in term of the Sigma and C14 structures; the RBA model results are shown in Figs. 2III and 2IV, respectively. The energy differences between complex phases (B2, Sigma or C14) and the BCC phase calculated using RBA as a function of *n* are shown in Figs. 2I-IV(a). The relationship between the calculated total energy difference between two competing structures (Eq. 3) and the plots of Fermi energy differences, $\Delta\varepsilon_F$ shown in Figs. 2I-IV(b) will be explained later in the "*Discussion*" section. The corresponding XRD patterns for CCFN and the four CCFN-A_X HEAs are presented in Figs. 2I-IV(c). Peaks observed were attributed to different possible phases: FCC, BCC, B2, Sigma and C14. In order to compare the theoretical RBA results and the experimental data, the valence electron concentration values *n* calculated within the RBA model for a chosen measured alloy composition are indicated on Figs. 2I-IV(a) and Figs. 2I-IV(b) by dashed lines of the same pattern as in the XRD results in Figs. 2I-IV(c).

The FCC-BCC energy difference for CCFN-Pd_x HEA obtained using the RBA method shows that the increase of *n* associated with the increasing additions of Pd, stabilises the FCC phase, see Fig. 2I(a).

Moreover, the region of stability of single FCC phase contains not only the CCFN and CCFN-Pd_x HEA compositions but it can be extended to *n* = 7. The experimental XRD results for corresponding valence electron concentration values, *n,* confirm the RBA prediction for the CCFN-Pd_x HEA since all of the patterns are indexed as the FCC phase. The experimental results also show an increase in the FCC lattice parameter with increasing concentration of Pd, which is in agreement with the most recent fully-relaxed DFT calculations[42].

Fig. 2II displays the results for RBA analysis for CCFN-Al_x where *x* = 0, 0.5, 1.0, and 1.5. The B2 phase is also considered as there is shown to be a high enthalpy of formation of the B2 structure between FeAl, CoAl, NiAl[43]. Moving down Figures 2II (a), (b), and (c) represents an increase in aluminium content according to corresponding *n* values, and the existence of the B2 phase for CCFN-$Al_{1.0}$ (*n* =7.2) and CCFN-$Al_{3.0}$ (*n* = 6.81) is confirmed through XRD verification which is also in accordance with the literature[31,32] while CCFN-$Al_{0.5}$ (*n* = 7.67) retains the FCC phase.

In Fig. 2III, for CCFN-V_x where *x* = 0, 0.3, 0.8, 1.0, and 2.0, we include consideration of the complex Sigma phase, shown in binary FeCr and FeV phase diagrams[44]. The valence electron concentration value n decreases with increasing V addition. By comparing Fig. 2III (a) and Fig. 2III (c), excellent agreement between experiment and stable phases predicted from ΔE_{Mag} values as a function of n is found, from single FCC to complex Sigma phase, in accordance with literature[35].

In Fig. 2IV, for CCFN-Ti_x where *x* = 0, 0.4, 0.6, 1.0, and 1.5, the C14 phase is additionally considered as an intermetallic structure related to the $CoTi_2$, $CrTi_2$, and $TiCr_2$ complex phase-forming binary compounds[44]. The inclusion of Ti and the related C14 complex phase into the RBA analysis destabilises the BCC phase much further below *n* = 5.5 than in the previously considered cases of Pd, Al and V alloying. XRD results show that CCFN-Ti undergoes a transition from the FCC to C14 phase between CCFN-$Ti_{0.6}$ (*n*=7.70) and CCFN-$Ti_{1.0}$ (n=7.40); the CCFN-$Ti_{1.0}$ (n=7.40), CCFN-$Ti_{1.5}$ (n=7.09), and CCFN-$Ti_{2.0}$ (*n*=6.83) phases have been indexed as FCC-C14, C14, and C14-BCC respectively. The structural trend reflecting changes in phase stability between FCC, C14 and BCC will be discussed in the next section.

Generally, the present predictions of phase stability as a function of *n* based on the RBA analysis have been found to give a reasonable match when compared to the outputs from our XRD analysis. Lowering of the value of *n* within families of HEAs causes a change in stability from a FCC single phase to complex phases (B2, Sigma and C14) back to a BCC single phase. Formation of complex phases is therefore observed close to the transition between FCC and BCC phases, located near *n* = 7 as observed in Fig. 1 for the CCFN alloys. This prediction, based on electronic structure calculations, agrees with Gao's empirical rules[12] where complex phase formation is suggested to occur at intermediate n values between 6.5 and 7.5.

Discussion

Electronic Origin of Phase Stability of Complex Phases in HEA.

In order to understand the structural trend from simple to complex phases in CCFN-A_x HEAs investigated in the previous section, we begin the analysis of phase stability of CCFN-Al_x (where *x* = 0.5, 1.0, and 3.0) within the RBA model by predicting the transition from the FCC to the B2 phase. It is worth emphasizing again that the RBA has been successfully applied to the investigation of structural trends in intermetallic compounds and complex Hume-Rothery phases in transitional metal aluminides known as *spd electron phases*[19,21]. Here the hybridisation effect between sp-valence electrons of Al with the d-orbitals of transition metals (TM) plays a crucial role in structural stability trends and their physical properties. In the case of CCFN-Al_x HEAs, a similar effect can be seen from the construction of frozen-potential approximation for Al and TM atoms (Cr, Co, Fe, Ni) to the electronic structure calculations within the RBA model for different SQS structures. It is well-

known from both experimental and DFT data that among the B2 compounds formed between Al and TMs, the B2-AlNi phase has the strongest negative enthalpy of formation[43]. The B2 phase can be constructed, therefore, from an ordered structure with four Al, Ni, Fe, Co atoms where Al-Ni pairs are dominant at nearest neighbour distances in the BCC-like structure.

Fig. 2IIa shows the B2-BCC structural energy difference calculated from the RBA model plotted together with the FCC-BCC difference as a function of *n*. It is found from the RBA calculations that competition between the FCC and B2 phases starts at valence electron concentration, $n \approx 8$. Comparison with the present experimental data for CCFN-$Al_{0.5}$ (*n* = 7.67) where FCC peaks are indicated in XRD (Fig.IIc), shows that the RBA model may overestimate the stability of the B2 phase. However, in comparison with a new HEA composition, $AlCoCrFeNi_{2.1}$, where the corresponding valence electron concentration is *n* = 7.70, the experimental observation[45] of an FCC/B2 dual-phase constitution not only validates our theoretical prediction but also demonstrates that the formation of B2 phase is strongly correlated with the short-range chemical order between Al and the excess composition of Ni transition metals in the HEAs.

The phase stability trends involving the FCC phase and intermetallic phase C14 for the CCFN-Ti_x compositions in Fig. 2IV also deserve further analysis. From Table 1, we observe a change in experimentally determined phase stabilities from CCFN-$Ti_{1.0}$, CCFN-$Ti_{1.5}$ and CCFN-$Ti_{2.0}$ as a mixture of FCC-C14, to C14, and finally a BCC-C14 mixture, respectively. By comparing the theoretical results displayed between Fig. 2IV and Fig. 1, it is found that the CCFN-$Ti_{1.0}$ composition with *n* = 7.40 is located within the CCFN FCC stable region while the CCFN-$Ti_{2.0}$ composition with *n* = 6.83 is below the CCFN FCC-BCC nodal point at *n* = 7.26. The CCFN-$Ti_{0.5}$ composition with *n* = 7.09 lies closest to the FCC-BCC nodal point where $\Delta E_{Mag} = 0$, suggesting that complex phases form at these points, which is in line with the analysis performed by Dominguez *et al.*[14] where the stability was found to range from the simple FCC phase (high VEC values), to complex phases (medium VEC values), to the simple BCC phase (low VEC values).

Relative Structural Stability and their Fermi Energy Difference, $\Delta \varepsilon_F$.

The relative structural stability of two phases within the RBA model is defined by comparing the spin-polarised band-structure energy difference in equation (3) as a function of the valence electron concentration, *n*, determined from equation (2). The origin of the structural stability within the RBA model can be further analysed in terms of the change in the Fermi energy[19,20]. This can be defined as the first derivative of the band energy difference of two competing structures with respect to the change in *n*:

$$\Delta \varepsilon_F^{(1-2)} = \frac{\partial\left(\Delta E_{Mag}^{(1-2)}\right)}{\partial n} \tag{4}$$

From equation (4) it follows that an extremum of the energy difference, ΔE_{Mag} occurs for the number of electrons at which the two Fermi energies are equal, i.e. $\Delta \varepsilon_F^{(1-2)} = 0$. This condition is important because it corresponds to points where the second phase becomes more stable in comparison to the first phase[19,20]. For the CCFN case shown in Fig. 1, $\Delta \varepsilon_F^{(FCC-BCC)} = 0$ at *n* = 5.5 where $\Delta E_{Mag}^{(FCC-BCC)}$ is a maximum and the BCC phase exhibits the largest stability with respect to the FCC phase, see Figs. 1(b) and 1(c). Applying the criterion (4) to CCFN-Pd_x, the maximum difference between FCC and BCC phase is predicted at *n* = 9.4, where $\Delta \varepsilon_F = 0$, as can be seen in Fig. 2I(b). For that value of *n* the FCC phase is more stable in comparison with the BCC phase.

Fig. 2II (b) shows $\Delta\varepsilon_F$ plots calculated from the energy difference ΔE_{Mag} for both the FCC and B2 phases in CCFN-Al_x HEA in reference to the BCC phase. The maximum difference ΔE_{Mag} between the FCC-BCC phases is at *n* = 7.8, which in turn corresponds to $\Delta\varepsilon_F = 0$, but the former is not the most stable structure since ΔE_{Mag} of the B2-BCC phases is lower than that of FCC-BCC phases at this value, as shown in Fig. 2II (a). A plot of $\Delta\varepsilon_F$ as a function of *n* for B2-BCC phases shows that there are two zero values at *n* = 6.4 and 7.4 where the B2 phase could be the most stable. The differentiation between these phases with XRD as used in the present study cannot be certain due to the low intensity of the peaks, but B2 formation appears to begin from CCFN-$Al_{0.5}$ (*n* = 7.67) and continues in CCFN-$Al_{1.0}$ (*n* = 7.2) and CCFN-$Al_{1.5}$ (*n* = 6.81). This agrees with the determined value of *n* = 7.4, where the Fermi energy difference between B2 and BCC is equal to zero. It is worth highlighting that by looking at the general competition between FCC, B2 and BCC phases the criterion $\Delta\varepsilon_F = 0$ strongly supports the experimental observation of dual FCC/B2 phases observed in $AlCoCrFeNi_{2.1}$ at *n*=7.7, which is located between the FCC stable phase (*n*=7.8) and the B2 stable phase (*n*=7.4).

For CCFN-V from Fig. 2III (b) it appears that for the maximum stability of the Sigma phase with respect to the BCC phase, two zero values for $\Delta\varepsilon_F$ at *n* = 7.65 and *n* = 6.65 are observed. From XRD results it is evident that the Sigma phase is dominant between CCFN-$V_{1.0}$ and CCFN-$V_{2.0}$ (*n* = 7.6 and *n* = 7.16 respectively), and CoFN-$V_{1.5}$ and CoFN-$V_{2.0}$ (*n* = 7.67 and *n* = 7.4, respectively). This is also close to the predicted value of the most stable Sigma at *n* = 7.65.

According to Fig. 2IV (b) for the CCFN-Ti family, the predicted stationary point of $\Delta\varepsilon_F = 0$ from the FCC-BCC plot, corresponding to the most stable FCC point, lies at *n* = 9.0. The stationary point for the C14-BCC plot is located at *n* = 6.4 where the C14 phase is most stable. The C14 phase is not observed as a stable structure of CCFN-$Ti_{0.4}$ at *n* = 7.85 and CCFN-$Ti_{0.6}$ at *n* = 7.7 because from Fig 2IV (a) ΔE_{Mag} of the FCC-BCC plot is lower than the C14-BCC one for *n* ≥ 7.69. It is possible that C14 phases may exist in small quantities and further precipitation is being supressed by the high cooling rate as a result of the synthesis method used in this work.

Thus, beside the case of CCFN-Pd_x HEA, where the FCC phase is the most stable for all n values (see Fig. 2I(b)), the above analysis using the criterion $\Delta\varepsilon_F = 0$ allows compositions to be predicted in CCFN-Al_x, CCFN-V_x, CCFN-Ti_x HEAs where complex phases are stable and these alloy families therefore possesses the ability to develop microstructures consisting of simple/complex phase combinations.

RBA versus Experimental observation of HEA Phase Stability as a Function of n

Fig. 3 shows a comparison of the experimentally-determined phase present and quantum-mechanical RBA-determined stable phase for each HEA family with different values of *n*. The first row for each HEA family represents the former as determined from ΔE_{Mag} while the indicated (bolded, underlined) regions show the points at which $\Delta\varepsilon_F = 0$ where the indicated phase is the most stable. It is shown that the agreement between experimental and RBA results is very satisfactory. In the case of CCFN-Al_x, the present experimental XRD results of the BCC phase in the range of Al concentration between 0.5 (*n*=7.67) and 1.0 (*n*=7.2) show that these alloys are strongly disordered, whereas the Al-Ni short range chemical-order alloys present within the RBA model are more in favour of the B2 phase. The experimental observation of dual FCC/B2 phases in the Ni-rich HEA of $AlCoCrFeNi_{2.1}$ (*n*=7.70) has confirmed the validity of the RBA prediction. In general, it is observed that the simple FCC phase is present at *n* > 8, complex phases are present between 6 < *n* < 8, and the simple BCC phase at *n* < 6. This variation in phase stability as a function of *n* supports the

simple two dimensional plots presented by Dominguez *et al.*[14] and Guo *et al.*[12]. In particular, the empirical VEC parameter used in all previous studies has a strong relationship with the quantum-mechanical value *n* from electronic-structure calculations.

Family	Method	5.0 -	5.5 -	6.0 -	6.5 -	7.0 -	7.5 -	8.0 -	8.5 -	9.0
CCFN	Exp.								FCC*	
	RBA	BCC	**BCC**	BCC	BCC	BCC	BCC	FCC	**FCC**	FCC
CCFN-Pd	Exp.								FCC*[30]	FCC*[30]
	RBA	**BCC**	BCC	BCC	BCC	BCC	FCC	FCC	FCC	**FCC**
CCFN-Al	Exp.				B2*[31,32]	B2*[31,32]	B2*[31,32]	FCC* FCC/B2[45]		
	RBA	BCC	B2	B2	B2	**B2**	B2	B2	FCC	FCC
CCFN-V	Exp.					σ*	σ*[33]	FCC*		
	RBA	BCC	BCC	σ	σ	σ	**σ**	FCC	FCC	**FCC**
CoFN-V	Exp.					σ*	FCC*	FCC*		
	RBA	BCC	BCC	σ	σ	σ	**σ**	FCC	FCC	**FCC**
CCFN-Ti	Exp.				C14*	C14*[34]	FCC*			
	RBA	C14	C14	**C14**	C14	C14	FCC	FCC	FCC	**FCC**

Figure 3. Phases present via XRD (Red) as a function of regions of valence electron concentration and predicted via ΔE_{Mag} (Black) and $\Delta \varepsilon_F = 0$ (**Bold, Underlined**) as a function of regions *n*. Both VEC and *n* are considered equivalent here, showing good interchangeability between both. While ΔE_{Mag} predicts the relative stability of different phases (*c.f.* equation (3)), $\Delta \varepsilon_F = 0$ represents the criterion point at which the considered phase is the most stable one (*c.f.* equation (4)). * indicates experiments performed in this work, while a superscript number indicates that the composition is found in the corresponding reference from the literature possessing the indicated structure.

It is apparent from Fig. 2 and summarised in Fig. 3 that performed in conjunction, analysis of ΔE_{Mag} and $\Delta \varepsilon_F$ results allow for deeper understanding of phase stabilities, although for rough predictions ΔE_{Mag} alone is enough to give relatively accurate results for the compositions tested in this work. A comparison of ΔE_{Mag} and $\Delta \varepsilon_F$ with *n* values for the tested compositional families show that in terms of phase stability, *n* at which the simple FCC phase transition is located is dependent on the chemical bonding nature of the alloying element to CCFN.

The results of the RBA analysis suggest that empirical VEC values have a strong connection to the values of *n* calculated from electronic spin-polarised DOS (Eq. 2) and that the accuracy of predictions in alloy design can be improved as long as electronic structure effects at the quantum scale are accounted for. In light of the dependency on the electronic structure, the increased accuracy with which HEA complex phases may be determined is not surprising. As Miedema's empirical rule for the enthalpy of mixing, ΔH, has been found to be inconsistent with quantum mechanical principles[46,47], the ability of the two-dimensional plot shown by Dominguez *et al.*[14] to distinguish between components may arise from the deviation in the ratio between the enthalpy of mixing and the difference in the number of valence electrons squared from Miedema's model. The latter quantity $\Delta H / (\Delta n)^2$ has been shown[47] to start deviating from theoretical predictions between $4 < n < 7$, which intersects with what are regarded as zones of complex phase presence in HEAs.

These factors may be accounted for by utilising the RBA technique presented in this paper. As shown in Fig. 2 and Fig. 3, ΔE_{Mag} values may be used to approximate, to a good degree of accuracy, the phases present in any particular stoichiometric composition within a preselected CCFN family (here family refers to all elemental alloying components comprising the composition), as a function of *n*.

Structural Stability of the New HEAs: CoFeNi-V_x

The above hypothesis is tested through the removal of Cr from CCFN-V_x to form CoFeNi-V_x (here denoted as CoFN-V_x) alloys and the analysis of phase stabilities utilising the RBA method as a function of changes in vanadium addition. To achieve this, we modify the CCFN FCC-BCC RBA analysis to include consideration of the Sigma phase due to strong enthalpies of mixing of FeCr and FeV for the Sigma phase, as in the case of CCFN-V_x. No explicit consideration is necessary as Co, Cr, Fe, Ni, and V are located on the same row of the periodic table.

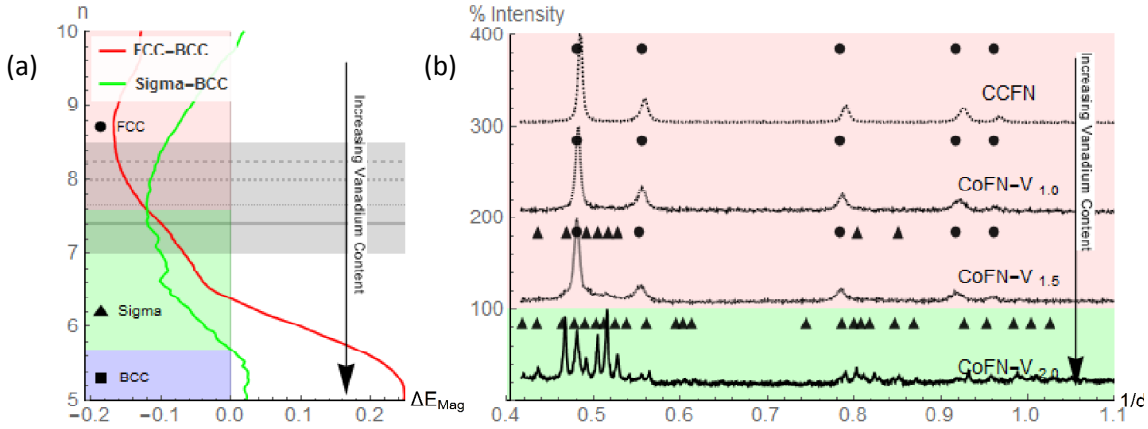

Figure 4. Transition of FCC to Sigma phase stability in CoFN-V (a) As a function of increasing Vanadium content represented by n, and (b) Its associated XRD Patterns.

Fig. 4 indicates the analysis of the CoFN-V_x composition, in terms of *n*. The RBA analysis described in Fig. 2(III) for the relative structural energy between FCC-BCC and FCC-Sigma phases in CCFN-V_x is adapted for investigation of the new HEAs. Removal of Cr has the effect of shifting *n* values to higher regions, with the effect of destabilising the Sigma structure. This shift in *n* to the region of FCC stability may be attributed to the Fermi surface nesting in HEAs with or without Cr which can stabilise a complex phase[48]. For equiatomic CoFN-$V_{1.0}$ at *n* = 8 we observe from Fig. 4 (a) that the FCC phase is stabilised as compared to the presence of Sigma phase previously considered at equiatomic CCFN-$V_{1.0}$ with *n* = 7.6. In Fig. 4 (b) experimental XRD patterns verify the prediction of CoFN-$V_{1.0}$ and subsequent compositions, CoFN-$V_{1.5}$ (FCC phase at *n*=7.67) and CoFN-$V_{2.0}$ (Sigma phase at *n*=7.40) predicted within the RBA model, indicating that the VEC values in Table 1 are in good agreement with *n* and that the RBA method therefore can be used as a valid tool for phase prediction, by taking into consideration the chemical bonding of the alloying species.

The power of the RBA model when used in conjunction with *n* in predicting complex phase formation in HEAs makes it suitable for the design of new HEA compositions. The relative phase stability as a function of *n* may be analysed for equiatomic compositions of designated multi-component alloys with four or more elements. As formation of the complex phase is identified to occur around the nodal points of FCC-BCC energy difference where $\Delta E_{Mag} = 0$ (*c.f.* Fig. 2), the generalisation of the RBA approach would require a starting alloy composition that is a known simple phase (FCC/BCC) such as CCFN (FCC), CCFN-Pd (FCC), CCFN-Mn (FCC), WNbMoTa (BCC), or TiVMnNb (BCC), which is then modified by changing its stoichiometry, or by further alloying additions to the composition. It is preferable for the initial structure to be FCC-type as it is less complicated to obtain the self-consistent charge density from a close-packed structure as an input frozen potential for the RBA, as compared to a more complex structure. The secondary phase chosen for consideration will depend on the alloying additions and the enthalpies of mixing of the phases, which may either be analysed directly or obtained from literature.

This alloy development strategy could become a platform to analyse specific compositions of interest and explore the effects of further additions on that particular system along the entire compositional range. Furthermore, phases of particular interest, such as the Laves phase for high-temperature structural materials, may be used as a starting point. The vast choice of combinations from within the periodic table could further diversify the compositions and provide strategies to optimise the mechanical properties, such as by changing the phase fraction and composition, or by including specific elements that individually would be possibly expected to improve chemical properties such as corrosion resistance (Cr, Mo), radiation shielding alloys (W), or biocompatibility (Pd) etc.

Conclusions

In this paper we have applied the RBA approach that gives a full description of the influence of electronic structure effects on phase formation in HEAs, and compared the predictions to experimental results. Our main findings are as follows:

a. The RBA model proves successful in predicting phases present in multicomponent HEAs as a result of macro alloying of the CCFN composition. The formation of complex phases is found to coincide with the transition between FCC and BCC, being the lower energy structures at intermediate values of the valence electron concentration, *n* determined from the integration of spin-polarised DOS computed for magnetic HEAs.

b. Values of *n*, for which complex phases are found, were predicted with more precision for specific alloy systems, and predictions were validated experimentally: the Sigma phase for CCFN-V_x ($n < 7.6$), B2 for CCFN-Al_x ($n < 8.1$) and C14 phase for CCFN-Ti_x ($n < 7.7$).

c. The RBA scheme is successful in predicting the presence of complex Sigma phase in the previously unreported CoFN-V_x composition ($n \leq 7.6$) and allows the prediction of other complex intermetallic phases in various new alloy compositions as a function of *n*. A design strategy based on this approach would be that through a careful selection of elements and/or utilising a known HEA composition with high *n* as a 'base' phase (FCC), it would be possible to include elements of interest for purposes such as corrosion resistance, biocompatibility, and high-temperature resistance, while mechanical properties could be influenced by changing the phase fraction and composition.

Methods

Sample Preparation

Samples were prepared by arc-melting elements of at least 99.9% purity in a water-cooled copper hearth in an argon atmosphere. The ingots were re-melted three times for good mixing and sectioned in half to be visually inspected for segregation. Samples with segregation or unmelted constituents were re-melted a further three times until good mixing was achieved. Following this the samples were then suction-cast as 3 mm diameter rods in a water-cooled copper mould.

X Ray Diffraction (XRD) Characterisation

Transmission XRD experiments of powder produced by rasping samples in the as-cast condition were conducted on a STOE Stadi diffractometer utilising a Mo k-α monochromated source. This method was chosen to allow characterisation of samples that proved to be brittle. Through comparison of experimental data with equivalent literature data it was found that similar phases present in the XRD pattern despite the lower resolution of the radiation source. All samples were run from 17° - 50° with a step size of 0.02 for four hours and the XRD patterns were Rietveld refined using reference instrument diffraction profiles.

All XRD values are presented as a function of the percentage intensity and reciprocal lattice, d^{-1}. Characterisation of the XRD results was performed utilising indexed patterns from the PDF4+ database as a guide; following which a Rietveld refinement on the lattice parameters and structure was performed on the data using the GSAS software package.

It should be recognised that, while commonly used for characterisation of the structure of metals and alloys, standard XRD may not detect lower intensity peaks associated with smaller phase fractions due to low resolution or poor signal-to-noise ratios, and also may not discriminate precisely between such effects as depth profile information and compositional variation from segregation, for example. However, for the current goal it is a suitable characterisation method as the RBA technique is itself a DFT-based electronic structure method suitable for predictions in situations of incomplete knowledge, and a complete experimental investigation of structure and properties would naturally follow.

Computational details

The frozen potential calculations have been performed using full-potential linear muffin-tin orbital LMTO code[28] allowing the self-consistent potentials DFT calculations to be carried out for RBA investigation. For each considered CCFN-based alloy both non-magnetic and spin-polarised electronic densities of states were obtained in order to predict the effective Stoner parameter, and the band energies and average magnetic moments as functions of the number of valence electrons per atom respectively. The investigated structures were assumed to be either fully disordered for the simple FCC and BCC phases or partially disordered for the complex B2, C14 and Sigma phases, where the chosen elements were preferentially occupying one of the sub-lattices. These structures were generated by using the special-quasi random structures method[29,30]. The Wigner-Seitz (WS) spheres in FCC, BCC, B2, and Sigma phases were assumed to be equal for different atomic species whereas in the C14 phase the WS spheres occupied by Cr atoms were assumed to be larger than others. Further details on the RBA may be found in the attached Supplementary Information.

Acknowledgements

This study has been funded by the EU FP7/AccMet project. The authors would like to further acknowledge Mr. P. Hawksworth for help in the experimental aspects of the work. DNM would like to acknowledge the International Fusion Energy Research Centre (IFERC) for providing access to a supercomputer (Helios) at Computational Simulation Centre (CSC) at Rokkasho (Japan). This work was also part-funded by the RCUK Energy Programme [grant number EP/I501045] and was carried out partly within the framework of the EUROfusion Consortium and has received funding from the Euratom research and training programme 2014-2018 under grant agreement No 633053. The views and opinions expressed herein do not necessarily reflect those of the European Commission.

References

1. Cantor, B., Chang, I. T. H., Knight, P. & Vincent, A. J. B. Microstructural development in equiatomic multicomponent alloys, Materials Science and Engineering A. *Phys. Rev. B Condens. Matter* **375–377,** 213–218 (2004).
2. Cantor, B. Multicomponent and High Entropy Alloys. *Entropy* **16–19,** 4749–4768 (2014).
3. Yeh, J. W. *et al.* Nanostructured high-entropy alloys with multiple principal elements: Novel alloy design concepts and outcomes. *Adv. Eng. Mater.* **6,** 299–303 (2004).
4. Zhang, Y. *et al.* Microstructures and properties of high-entropy alloys. *Prog. Mater. Sci.* **61,** 1–93 (2014).
5. Santodonato, L. J. *et al.* Deviation from high-entropy configurations in the atomic distributions of a multi-principal-element alloy. *Nat. Commun.* **6,** 5964 (2015).
6. Yeh, J. W. Recent progress in high—entropy alloys. *Ann. Chim. - Sci. Mater.* **31,** 633–648 (2006).
7. Otto, F., Yang, Y., Bei, H. & George, E. P. Relative effects of enthalpy and entropy on the phase stability of equiatomic high-entropy alloys. *Acta Mater.* **61,** 2628–2638 (2013).
8. Pickering, E. J., Munoz-Moreno, R., Stone, H. J. & Jones, N. G. Precipitation in the equiatomic high-entropy alloy CrMnFeCoNi. *Scr. Mater.* **113,** (2016).
9. Cornide, J. *et al.* Combined atom probe tomography and TEM investigations of CoCrFeNi, CoCrFeNi-Pdx (x=0.5, 1.0, 1.5) And CoCrFeNi-Sn. *Acta Phys. Pol. A* **128,** (2015).
10. Dahlborg, U. *et al.* Crystalline structures of some high entropy alloys obtained by neutron and x-ray diffraction. *Acta Phys. Pol. A* **128,** (2015).
11. Hume-Rothery, W., Smallman, R. E. & Haworth, C. W. *The Structure of Metals and Alloys*. (The Institute of Metals, 1988).
12. Guo, S., C, N., J, L. & T, L. C. Effect of valence electron concentration on stability of fcc or bcc phase in high entropy alloys. *J. Appl. Phys.* **109,** 10 (2011).
13. Poletti, M. G., Fiore, G., Szost, B. A. & Battezzati, L. Search for high entropy alloys in the X-NbTaTiZr systems (X = Al, Cr, V, Sn). *J. Alloys Compd.* **620,** 283–288 (2015).

14. Dominguez, L. A., Goodall, R. & Todd, I. Prediction and validation of quaternary high entropy alloys using statistical approaches. *Mater. Sci. Technol.* **31,** 1201–1206 (2015).
15. Zhang, Y., Yang, X. & Liaw, P. K. Alloy design and properties optimisation of high-entropy alloys. *J. Mater. Miner. Min. Soc.* **64,** 830–838 (2012).
16. Kohn, W. & Sham, L. J. Self-Consistent Equations Including Exchange and Correlation Effects. *Phys. Rev.* **140,** A1133–A1138 (1965).
17. Troparevsky, M. C., Morris, J. R., Kent, P. R. C., Lupini, A. R. & Stocks, G. M. Criteria for Predicting the Formation of Single-Phase High-Entropy Alloys. *Phys. Rev. X* **5,** (2015).
18. Kormann, F. *et al.* 'Treasure maps' for magnetic high-entropy-alloys from theory and experiment. *Appl. Phys. Lett.* **107,** (2015).
19. Nguyen-Manh, D., Paxton, A., Pettifor, D. G. & Pasturel, A. On the phase stability of transition metal trialuminide compounds. *Intermetallics* **3,** 9–14 (1995).
20. Paxton, A., Methfessel, M. & Pettifor, D. G. A bandstructure view of the Hume-Rothery electron phases. *Proc. R. Soc. A* **453,** 1493 (1997).
21. Trambly de Laissardière, G., Nguyen-Manh, D. & Mayou, D. Electronic structure of complex Hume-Rothery phases and quasicrystals in transition metal aluminides. *Prog. Mater. Sci.* **50,** 679–788 (2005).
22. Nguyen-Manh, D., Vitek, V. & Horsfield, A. P. Environmental dependence of bonding: A challenge for modelling of intermetallics and fusion materials. *Prog. Mater. Sci.* **52,** 52 (2007).
23. Liu, G., Nguyen-Manh, D., Liu, B. G. & Pettifor, D. G. Magnetic properties of point defects in iron within the tight-binding-bond Stoner model. *Phys. Rev. B* **71,** 174115 (2005).
24. Nguyen-Manh, D. & Dudarev, S. L. Model many-body Stoner Hamiltonian for binary FeCr alloys. *Phys. Rev. B* **80,** 104440 (2009).
25. Dudarev, S. L. & Derlet, P. M. Interatomic potentials for materials with interacting electrons. *J. Comput.-Aided Mater. Des.* **14,** 129 (2008).
26. Kübler, J. K. *Theory of itinerant electron magnetism*. (Oxford University Press, 2009).

27. Derlet, P. & Dudarev, S. Million-atom molecular dynamics simulations of magnetic iron. *Prog. Mater. Sci.* **52,** 299–318 (2007).
28. Wrobel, J. S., Nguyen-Manh, D., Lavrentiev, M. Y., Muzyk, M. & Dudarev, S. L. Phase stability of ternary fcc and bcc Fe-Cr-Ni alloys. *Phys. Rev. B* **91,** 21408 (2015).
29. Niu, C. *et al.* Spin-driven ordering of Cr in the equiatomic high entropy alloy NiFeCrCo. *Appl. Phys. Lett.* **106,** 161906 (2015).
30. Lucas, M. S. *et al.* Magnetic and vibrational properties of high-entropy alloys. *J. Appl. Phys.* **109,** 7 (2011).
31. Chou, H. P., Chang, Y. S., Chen, S. K. & Yeh, J. W. Microstructure, thermophysical and electrical properties in Al x CoCrFeNi (0 ≤ x ≤2) high-entropy alloys. *Mater. Sci. Eng. B* **163,** 184–189 (2009).
32. Wang, W. R. *et al.* Effects of Al addition on the microstructure and mechanical property of AlxCoCrFeNi high-entropy alloys. *Intermetallics* **26,** 44–51 (2012).
33. Salishchev, G. A. *et al.* Effect of Mn and V on structure and mechanical properties of high-entropy alloys based on CoCrFeNi system. *J. Alloys Compd.* **591,** 11–21 (2014).
34. Shun, T. T., Chang, L. Y. & Shiu, M. H. Microstructures and mechanical properties of multiprincipal component CoCrFeNiTix alloys. *Mater. Sci. Eng. A* **556,** 170–174 (2012).
35. Pettifor, D. G. Pressure-cell boundary relation and application to transition-metal equation of state. *Commun. Theor. Phys.* **1,** (1977).
36. Andersen, O. K., Skriver, H. L., Nohl, H. & Johansson, B. J. Electronic structure of transition metal compounds; ground-state properties of the 3d-monoxides in the atomic sphere approximation. *Pure Appl. Chem.* **52,** 93 (1980).
37. Krier, G., Jepsen, O., Burkhardt, A. & Andersen, O. J. *The TB-LMTO-ASA program*. (Max-Planck-Institute für Festkörperforschung, 1994).
38. Zunger, A., Wei, S., Ferreira, L. & Bernard, J. Special quasirandom structures. *Phys. Rev. Lett.* **65,** (1990).

39. Walle, A. V. de *et al.* Efficient stochastic generation of special quasirandom structures. *Calphad - Comput. Coupling Phase Diagr. Thermochem.* **42,** 13–18 (2013).

40. Senkov, O. N., Wilks, G. B., Miracle, D. B., Chuang, C. P. & Liaw, P. K. Refractory high-entropy alloys. *Intermetallics* **18,** 1758–1765 (2010).

41. Toda-Caraballo, I., Wrobel, J. S., Dudarev, S. L., Nguyen-Manh, D. & Rivera-Diaz-del-Castillo, P. E. J. Interatomic spacing distribution in multicomponent alloys. *Acta Mater.* **97,** (2015).

42. Calvo-Dahlborg, M. *et al.* Effect of Pd on structural and magnetic properties of high entropy CoCrFeNiPd alloys. In preparation. (2016).

43. Nguyen-Manh, D. & Pettifor, D. G. Electronic structure, phase stability, and elastic moduli of AB transition metal aluminides. *Intermetallics* **7,** (1999).

44. *ASM Alloy Phase Diagrams Database*. (ASM International, 2006).

45. Lu, Y. *et al.* A Promising New Class of High-Temperature Alloys: Eutectic High-Entropy Alloys. *Sci. Rep.* **4,** 6200 (2014).

46. Pettifor, D. G. A Quantum Mechanical Critique of the Miedema Rules for Alloy Formation. *Solid State Phys.* **40,** 43–92 (1987).

47. Pettifor, D. G. Theory of the Heats of Formation of Transition-Metal Alloys. *Phys. Rev. Lett.* **42,** 846 (1978).

48. Stocks, G. M. *et al.* in (eds. Liu, C. T., Cahn, R. W. & Sauthoff, G.) 15–36 (Springer Netherlands, 1992).

49. Pettifor, D. G. Individual orbital contributions to the SCF virial in homonuclear diatomic molecules. *J. Chem. Phys.* **69,** 2930 (1978).

50. Jones, H. J. Concentrated solid solutions of normal metals. **23,** Journal de Physique et le Radium (1962).

51. Christensen, N., Gunnarsson, O., Jepsen, O. & Andersen, O. J. Local spin density theory for ferro- and antiferromagnetic materials. *J. Phys. C* **8,** (1988).

Supplementary Information

Rigid Band model

The structural stability of simple FCC and BCC phases, and all other complex phases observed in multi-component alloys can be investigated by using the frozen potential approximation (FPA) to density functional theory (DFT). Within the first order approximation the energy difference between any two non-magnetic structures is given by the difference between their band energies at a fixed equilibrium volume, V_0 [35,36,49]:

$$\Delta E_{Non-Mag}^{(1-2)} \approx \Delta E_{Band}^{(1-2)} = \left[2\int_{-\infty}^{\varepsilon_F^{(1)}} \varepsilon D^{(1)}(\varepsilon)d\varepsilon - 2\int_{-\infty}^{\varepsilon_F^{(2)}} \varepsilon D^{(2)}(\varepsilon)d\varepsilon\right]_{\Delta V_0=0} \quad \text{(I)}$$

where $D^{(1)}(\varepsilon)$ and $D^{(2)}(\varepsilon)$ are the densities of states (DOS) per atom with a factor of 2 for a spin to energy ε and $\varepsilon_F^{(1)}$ and $\varepsilon_F^{(2)}$ are the Fermi energies for structure 1 and 2, respectively. They are determined from the number of valence electrons per atom:

$$n = 2\int_{-\infty}^{\varepsilon_F^{(1)}} D^{(1)}(\varepsilon)d\varepsilon = 2\int_{-\infty}^{\varepsilon_F^{(2)}} D^{(2)}(\varepsilon)d\varepsilon \quad \text{(II)}$$

Frozen potentials for the different atomic species are determined from self-consistent calculations, normally for structures with a small unit cell. They are then transferred into other structures with the same alloy composition and the same equilibrium volume. The difference between the band energies $\Delta E_{Band}^{(1-2)}$ is calculated under the constraint that the potential within the Wigner-Seitz sphere remains unchanged (frozen) when going from one structure type to another. Since the energy difference in the first order frozen potential approximation is computed assuming fixed atomic volumes, this approximation is correct for structures with relatively similar equilibrium atomic volumes like for example FCC and BCC phases, which can be related to each other through the Bain transformation.

Assuming that alloying changes the number of valence electrons per atom but the electronic DOS of different phases remain rigid (the rigid band approximation), the variation of the energy difference as a function of the number of electrons can be evaluated by comparing the band energies, see equation (I)[19,20,50].

Within the present work, the RBA model has been generalised for the case of magnetic materials like CCFN-based alloys using the Stoner model of magnetism[23–27]. In transition metal alloys the latter one introduces magnetism by introducing local exchange fields within the band energy concept. In particular, electrons with spins up and down have different on-site energies depending on whether their spin is parallel or anti-parallel to the local magnetic moment. The effective on-site energy ε_i^σ is given by

$$\varepsilon_i^\sigma = \varepsilon_i \pm \frac{1}{2} I_i m_i \quad \text{(III)}$$

where ε_i is the single-particle non-magnetic on-site energy, $m_i = n_i^\downarrow - n_i^\uparrow$, is the difference between electron occupancies of site i by spin-down and spin-up electrons with a spin index σ. The Stoner exchange parameter I_i refers to the exchange splitting of on-site energies of electrons with spin up and spin down due to the local magnetic moment m_i [23,24,26,27,30].

From equation (III), the energy difference between two magnetic structures, following the Stoner model of magnetism (Stoner Model I), corrected for the double counting contribution, and normalised by the number of atoms, N in both structures can be given by:

$$\Delta E_{Mag}^{(1-2)} = \Delta E_{Spin-Band}^{(1-2)} + \frac{1}{4N}\left[\sum_i I_i^{(1)} m_i^{2(1)} - \sum_i I_i^{(2)} m_i^{2(2)}\right] \quad \text{(IV)}$$

where the first term is the spin-polarised band energy difference between any two magnetic structures at a fixed equilibrium volume V_0 (defined below in equation (V)), the second term is the double-counting contribution arising from magnetic interactions[23–25], and N is the number of atoms in both considered structures. $\Delta E_{Spin-Band}^{(1-2)}$ is defined as:

$$\Delta E_{Spin-Band}^{(1-2)} = \left[\int_{-\infty}^{\varepsilon_F^{(1)}} \left(\varepsilon D^{(1)\uparrow}(\varepsilon) + \varepsilon D^{(1)\downarrow}(\varepsilon)\right) d\varepsilon - \int_{-\infty}^{\varepsilon_F^{(2)}} \left(\varepsilon D^{(2)\uparrow}(\varepsilon) + \varepsilon D^{(2)\downarrow}(\varepsilon)\right) d\varepsilon\right]_{\Delta V_0 = 0} \quad \text{(V)}$$

where $D^{(1)\uparrow}(\varepsilon)$ and $D^{(2)\uparrow}(\varepsilon)$ are the spin-polarised total DOS per atom for electrons with spin-up and $D^{(1)\downarrow}(\varepsilon)$ and $D^{(2)\downarrow}(\varepsilon)$ are the spin-polarised total DOS per atom for electrons with spin-down. The Stoner parameters in equation (IV) are assumed to be constant for each type of atoms[51]**.** However, application of equation (IV) requires knowledge of the magnetic moments of all atoms as a function of *n* in the system, of which is difficult to be validated experimentally. Therefore, we use an effective Stoner parameter I_{eff} which refers to the exchange splitting of the on-site energies of electrons with spin-up and spin-down due to the average atomic magnetic moment m_{av}, defined as:

$$I_{eff}\, m_{av} = \varepsilon_F^{\downarrow} - \varepsilon_F^{\uparrow} \quad \text{(VI)}$$

where $\varepsilon_F^{\uparrow}$ and $\varepsilon_F^{\downarrow}$ are the Fermi energies for electrons with spin-up and spin-down, respectively, defined as energies of the non-magnetic total DOS, $D(\varepsilon)$, which are the number of electrons per atom with spin-up and spin-down, obtained from the spin-polarised total DOS. The average magnetic moment of the entire simulation cell from the non-magnetic total DOS is equal to the one obtained from the spin-polarised total DOS and is given by:

$$m_{av} = \int_{-\infty}^{\varepsilon_F} D^{\downarrow}(\varepsilon) d\varepsilon - \int_{-\infty}^{\varepsilon_F} D^{\uparrow}(\varepsilon) d\varepsilon = \int_{\varepsilon_F^{\uparrow}}^{\varepsilon_F^{\downarrow}} D(\varepsilon) d\varepsilon \quad \text{(VII)}$$

By using the effective Stoner parameter and the average magnetic moment the energy difference between any two magnetic structures in the effective Stoner Model II can now be written as:

$$\Delta E_{Mag}^{(1-2)} = \Delta E_{Spin-Band}^{(1-2)} + \frac{1}{4}\left[I_{eff}^{(1)} m_{av}^{2\,(1)} - I_{eff}^{(2)} m_{av}^{2\,(2)}\right] \quad \text{(VIII)}$$

Both Stoner Model I and effective Stoner Model II can be justified by the comparison of energy differences with those obtained using the LMTO code. As shown in Table SI the energy differences between the considered magnetic structures and the BCC structures with the same composition calculated using both equation (IV) and (VIII) are in quantitative agreement with each other and in line with the results calculated using the LMTO code. The only exception is that the C14 structure of $Co_9Cr_{12}Fe_9Ni_6$ alloy which is less stable than the BCC phase when equation (VIII) is applied and it is more stable than the BCC phase by using equation (IV) and the LMTO code. However, all the considered methods predict that the FCC phase is the most stable one.

Table SI. Average magnetic moments obtained using equation (VII) (m_{av}) and energy differences (ΔE_{mag}) between the considered magnetic structures and the BCC structures with the same composition calculated using equations (IV) and (VIII), compared with the results calculated using the LMTO code. I_{eff} is the effective Stoner parameters calculated using equation (VI). Energies, magnetic moments and effective Stoner parameters are given in eV , μ_β per atom and eV/μ_β, respectively. The valence electron concentration of considered structures is indicated by *n*.

	Structure	ΔE_{Mag} (equation (IV))	ΔE_{Mag} (equation (VIII))	ΔE_{Mag} (LMTO)	m_{av} (equation (VII))	m_{av} (LMTO)	I_{eff} (equation (VI))
CCFN $Co_8Cr_8Fe_8Ni_8$ (*n* = 8.25)	FCC	-0.136	-0.099	-0.083	0.372	0.372	1.295
	BCC				0.421	0.421	1.302
CCFN-Al $Co_8Fe_8Ni_8Al_8$ (*n* = 7.5)	FCC	-0.043	-0.020	-0.001	0.939	0.930	3.940
	BCC				1.011	0.990	4.392
	B2	-0.065	-0.102	-0.072	0.948	0.948	4.124
CCFN-Pd $Co_6Cr_7Fe_7Ni_6Pd_6$ (*n* = 8.5)	FCC	-0.139	-0.070	-0.064	0.881	0.864	3.631
	BCC				0.913	0.915	3.746
CCFN-V $Co_9Cr_{12}Fe_9Ni_6$ (*n* = 8.133)	FCC	-0.147	-0.123	-0.073	0.350	0.344	1.228
	BCC				0.415	0.422	1.205
	Sigma	-0.151	-0.120	-0.069	0.312	0.317	0.993
CCFN-Ti $Co_9Cr_{12}Fe_9Ni_6$ (*n* = 7.917)	FCC	-0.063	-0.027	-0.021	0.687	0.171	0.987
	BCC				0.691	0.172	0.831
	C14	-0.018	0.022	-0.013	0.817	0.819	0.909